Chemical Science

ROYAL SOCIETY OF CHEMISTRY

EDGE ARTICLE

View Article Online
View Journal | View Issue

Cite this: *Chem. Sci.*, 2026, **17**, 4601

All publication charges for this article have been paid for by the Royal Society of Chemistry

Exploring stacking pressure-induced mechanical failure of a Ni-rich cathode in sulfide solid-state batteries

Yiman Feng,[a] Zhixing Wang,[a] Gui Luo,[b] Duo Deng,[b] Wenjie Peng,[ab] Wenchao Zhang,[a] Hui Duan,[a] Feixiang Wu,[ac] Xing Ou,[a] Junchao Zheng[ac] and Jiexi Wang *[ac]

Received 28th November 2025
Accepted 19th December 2025

DOI: 10.1039/d5sc09321j

rsc.li/chemical-science

All-solid-state lithium batteries (ASSLBs) employing Ni-rich layered oxide cathodes (NRLOs) and sulfide solid-state electrolytes (SSEs) demonstrate high energy density and enhanced safety. However, the impact of stacking pressure on the mechanical failure of NRLOs is not well understood. This study systematically investigates the effect of stacking pressure on the chemo-mechanical degradation of NRLOs in sulfide ASSLBs separately with lithium indium (LiIn) and zero-strain lithium titanate (LTO) as anodes. Through multi-dimensional characterization and electrochemical testing, it is demonstrated that increased stacking pressure compresses interfacial voids and reduces lithium-ion transport resistance, significantly enhancing the performance of sulfide ASSLBs. Nevertheless, excessive stacking pressure induces significant stress concentration during cycling, exacerbating lattice distortion, oxygen release, and the decomposition of the sulfide SSE. These effects contribute to fragmentation of NRLO particles and interlayer cracking of electrodes, ultimately leading to severe capacity fade and increased impedance. The findings provide critical insights for optimizing stacking pressure in durable sulfide ASSLBs.

Introduction

The global pursuit of high-energy-density, safe, and long-cycle-life energy storage systems has driven rapid advancements in all-solid-state lithium batteries (ASSLBs).[1–3] Among these, sulfide solid-state electrolytes (SSEs) have emerged as a highly promising candidate.[4,5] In contrast to traditional lithium-ion batteries (LIBs) which rely on flammable liquid electrolytes, ASSLBs utilize sulfide SSEs that exhibit high ionic conductivity ($>10^{-3}$ S cm^{-1}), excellent compatibility with lithium metal anodes, and intrinsic resistance to thermal runaway.[6–9] These properties address critical safety concerns associated with LIBs while enabling higher energy density configurations. As a result, ASSLBs integrated with Ni-rich layered oxide cathodes (NRLOs, Ni content $\geq$80%) are recognized as the most promising electrochemical energy storage systems.[10,11] To mitigate the interfacial instability between sulfide SSEs and NRLOs, and further construct a stable cathode–electrolyte interface (CEI) layer, a range of effective coating materials for NRLOs have been proposed, such as Li_2O,[12] $LiNbO_3$,[13] Li_3PO_4,[14] $LiAlO_2$,[15] Li_3BO_3–Li_2CO_3,[16] and $Ti_3(PO_4)_4$.[17]

Despite the presence of a stable interface, the commercialization of sulfide ASSLBs is hindered by unresolved mechanical failure issues.[18–20] Active material particles exhibit varying degrees of expansion or contraction during the lithiation and delithiation process. For example, silicon anodes experience a volume expansion of 280–300% during their transformation into $Li_{4.4}Si$.[21,22] In contrast, the adoption of nanostructures (such as silicon nanoparticles and nanowires)[23] to buffer volume expansion, or the compositing of silicon with carbon materials, such as silicon/carbon composites,[24] can reduce the volume change to 150–200% and enhance the structural stability and cycle life. For cathode active materials (CAMs), lithium cobalt oxide (LCO) undergoes a volume expansion of approximately 2 vol% during discharge, followed by contraction during charging.[25] In comparison, NRLOs undergo much larger volume changes (typically 5–10 vol%) throughout the entire charging and discharging process, with the degree of contraction depending on their Ni content.[26,27]

In recent years, there has been a growing recognition of the influence of stacking pressure on the performance of sulfide ASSLBs.[28–31] However, the reported levels of stacking pressure in the literature vary significantly, spanning multiple orders of magnitude.[32] It is evident that the fundamental understanding of battery stacking pressure remains limited. Furthermore,

[a]*National Energy Metal Resources and New Materials Key Laboratory, Engineering Research Center of the Ministry of Education for Advanced Battery Materials, Hunan Provincial Key Laboratory of Nonferrous Value-Added Metallurgy, School of Metallurgy and Environment, Central South University, Changsha 410083, China. E-mail: wangjiexikeen@csu.edu.cn*

[b]*BASF Shanshan Battery Materials Co Ltd, Changsha 410205, China*

[c]*National Engineering Research Centre of Advanced Energy Storage Materials, Changsha 410205, China*

most current studies on stacking pressure focus on its impact on metallic lithium anodes. This is attributed to the high theoretical capacity of metallic lithium (3860 mAh g^{-1})[33] and the critical challenges it faces, such as dendrite growth, severe volume expansion (300–400% during lithiation),[34] and an unstable solid electrolyte interphase layer, all of which are highly sensitive to pressure.[30,31,35] Under these circumstances, the impact of stacking pressure on the mechanical failure of NRLOs in sulfide ASSLBs remains unclear due to the limitations of existing research methods. For instance, computational studies using finite element analysis (FEA)[25,31,36,37] have modeled cathode stress evolution, yet few have integrated real-time electrochemical data (*e.g.*, cyclic voltammetry (CV), electrochemical impedance spectroscopy (EIS)) to quantify how mechanical failure modulates ion transport kinetics. This gap underscores the need for a holistic approach that couples mechanical characterization with electrochemical testing to unravel the pressure-dependent failure mechanisms of NRLOs in sulfide ASSLBs.

Herein, this study systematically investigates the effect of stacking pressure on the electrochemical performance and mechanical behavior of the cathodes in sulfide ASSLBs. Using zero-strain lithium titanate (LTO) and lithium indium (LiIn) alloy as anodes, and combining techniques such as nano-computed tomography (CT), differential electrochemical mass spectrometry (DEMS), distribution of relaxation times (DRT) analysis and high-resolution transmission electron microscopy (HRTEM), the intrinsic relationship between stacking pressure, battery performance, and cathode failure is revealed. On the one hand, as stacking pressure increases, the voids at the solid–solid interface decrease, facilitating lithium ion (Li^+) migration and enhancing the discharge specific capacity and rate performance of sulfide ASSLBs. On the other hand, with the increase of stacking pressure, the significant volume effect of the anode in LiIn sulfide ASSLBs causes severe internal pressure fluctuations, which cause lattice distortion of NRLOs, increase in oxygen vacancies, and oxidative decomposition of the sulfide SSE, resulting in a rapid decay of battery performance. At 375 MPa, the LiIn sulfide ASSLB exhibits a capacity retention rate of only 29.2% after 100 cycles, and its discharge specific capacity at 2 C rate drops sharply to 45 mAh g^{-1}, representing a 50% decrease compared to that at 250 MPa. In contrast, the zero-strain characteristic of the LTO anode (volume change < 0.1%) results in mild pressure changes within the battery, allowing for a capacity retention of 68.4% after 100 cycles at 375 MPa, along with continuous improvement in rate capability.

Results and discussion

Fig. 1 shows the electrochemical performance of sulfide ASSLBs within a voltage range of 2.7–4.3 V *vs.* Li/Li^+ at 25 °C under different stacking pressures. Fig. 1a–c focuses on the LiIn sulfide ASSLBs, revealing a clear positive correlation between stacking pressure and initial discharge specific capacity. When the stacking pressure is increased from 125 MPa to 250 MPa and further to 375 MPa, the initial discharge specific capacity rises progressively from 195 mAh g^{-1} to 202 mAh g^{-1}, and finally to 207 mAh g^{-1}. A similar trend in initial discharge specific capacity is observed in LTO sulfide ASSLBs, as shown in Fig. 1f–h. When the stacking pressure increases from 125 MPa to 375 MPa, the initial discharge specific capacities of LTO sulfides are 179, 205 and 214 mAh g^{-1} respectively. Notably, the initial coulombic efficiency (ICE) exhibits significant differences between the two types of batteries. With increasing stacking pressure, the ICE of LiIn sulfide ASSLBs first increases and then decreases (Fig. 1a–c), while that of LTO sulfide ASSLBs continues to rise (Fig. 1f–h). The LiIn-375 MPa sulfide ASSLB even exhibits the phenomenon of overcharging and shallow discharging. Its initial charge specific capacity is as high as 279 mAh g^{-1}, yet its ICE is only 75.6%. In contrast, the ICE of the LTO-375 MPa sulfide ASSLB can reach 81.1%. Consistent with the experimental regularity obtained in this study, the work by RenJie Chen *et al.*[29] summarizes the relationship between stacking pressure and ICE in LiIn sulfide ASSLBs. It points out that the increase in stacking pressure establishes better interfacial contact; however, when the pressure exceeds a certain threshold, it leads to mechanical failure of ASSLBs, resulting in a rapid decline in ICE. Therefore, the mechanical failure threshold of LiIn sulfide ASSLBs is significantly lower than that of LTO sulfide ASSLBs, underscoring the importance of investigating the effect of stacking pressure on the mechanical failure of LiIn sulfide ASSLBs.

The rate performance was evaluated across a current density range of 0.1 C to 2 C. As shown in Fig. 1a–c and S4a, when the stacking pressure increases from 125 MPa to 250 MPa, the rate performance of the LiIn sulfide ASSLBs is significantly enhanced and the discharge specific capacity increases from 76 mAh g^{-1} to 91 mAh g^{-1} at 2 C. However, when the pressure is further increased to 375 MPa, the discharge specific capacity of the LiIn sulfide ASSLB at 2 C drops sharply to 45 mAh g^{-1}, demonstrating a decrease of nearly 50% compared to the 250 MPa condition. This dramatic decline signals severe degradation of ion transport kinetics under excessive pressure. To gain deeper insight into the kinetic changes, Fig. S4b illustrates the voltage drop of LiIn sulfide ASSLBs during discharge at different rates. Compared with the LiIn-125 MPa sulfide ASSLB, the LiIn-250 MPa sulfide ASSLB shows a noticeably lower voltage drop during discharge across all tested rates. This confirms reduced internal polarization of the battery and faster Li^+ ion transport kinetics. When the stacking pressure increases to 375 MPa, the voltage drop of the LiIn-375 MPa sulfide ASSLB rises sharply, suggesting that Li^+ ion transport is hindered and internal polarization is enhanced.[38] Different from LiIn sulfide ASSLBs, the LTO sulfide ASSLBs display a consistent positive correlation between stacking pressure and rate performance. As shown in Fig. 1f–h and S5a, their rate performance continues to improve as stacking pressure increases from 125 MPa to 375 MPa. Even at 2 C rate, the discharge specific capacity keeps rising without showing the decline like in the LiIn system. Correspondingly, Fig. S5b reveals that the voltage drop of LTO sulfide ASSLBs decreases continuously with increasing stacking pressure, which indicates the enhancement of Li^+ transport kinetics.

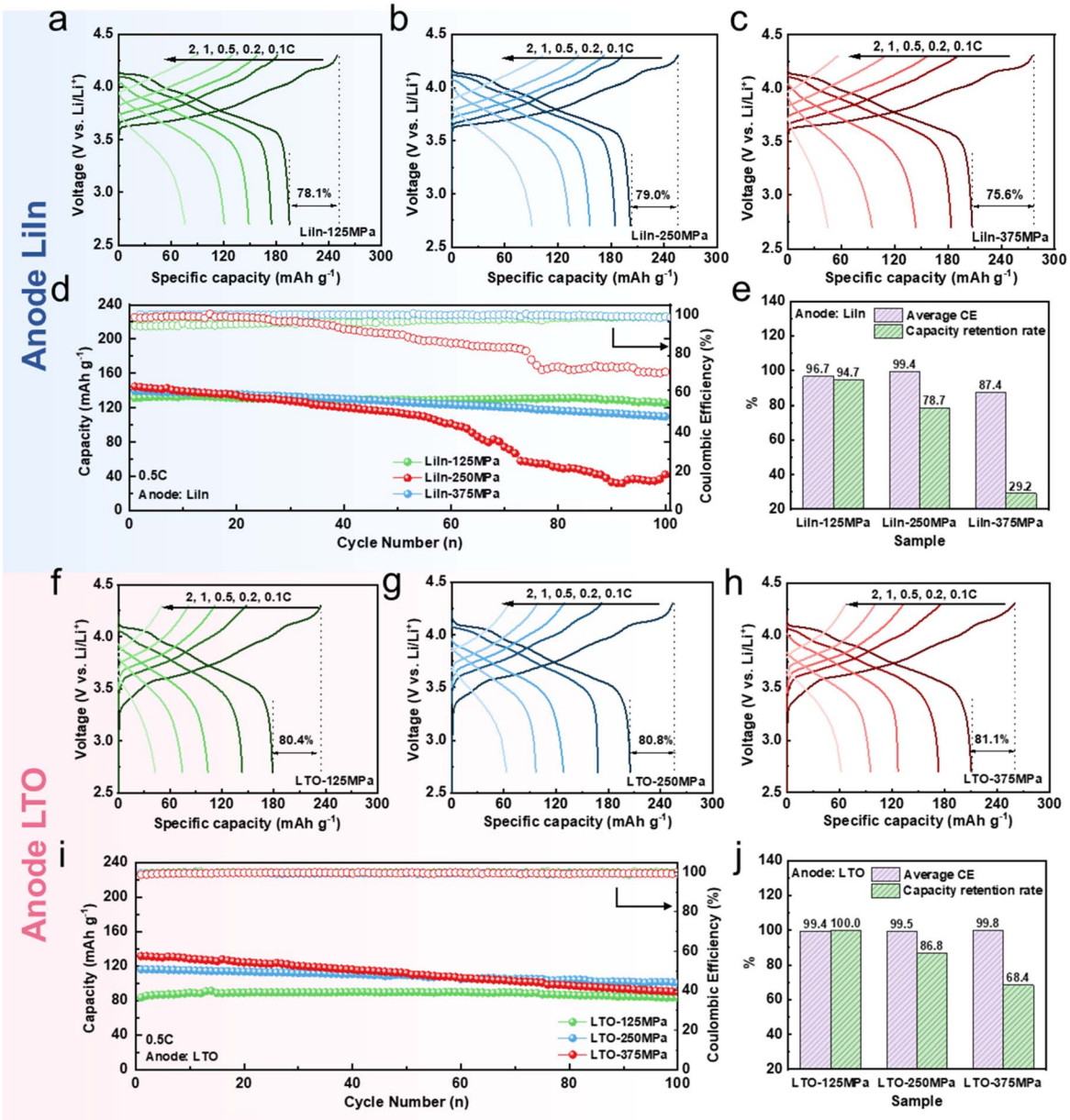

Fig. 1 Electrochemical performance of sulfide ASSLBs under different stacking pressures. The charge–discharge voltage profiles between 2.7 and 4.3 V *vs.* Li/Li^+ of (a) LiIn-125 MPa, (b) LiIn-250 MPa, and (c) LiIn-375 MPa sulfide ASSLBs at different rates. (d) Long-term cycling performance of LiIn sulfide ASSLBs with different stacking pressure at a rate of 0.5 C. (e) Average CE and capacity retention rate of LiIn sulfide ASSLBs with different stacking pressure. The charge–discharge voltage profiles between 2.7 and 4.3 V *vs.* Li/Li^+ of (f) LTO-125 MPa, (g) LTO-250 MPa, and (h) LTO-375 MPa sulfide ASSLBs at different rates. (i) Long-term cycling performance of LTO sulfide ASSLBs with different stacking pressures at a rate of 0.5 C. (j) Average CE and capacity retention rate of LTO sulfide ASSLBs with different stacking pressures.

Fig. 1d and i compare the cycling stability of the two types of sulfide ASSLBs under different stacking pressures. With increasing stacking pressure, the capacity retention rates of both batteries decrease. Notably, the LiIn-375 MPa sulfide ASSLB exhibits severe capacity loss after 50 cycles, and its capacity retention rate is only 29.2% after 100 cycles (Fig. 1d and e), indicating that the internal structure or interfacial stability has been significantly damaged. In contrast, the LTO-375 MPa sulfide ASSLB shows relatively better cycling performance over 100 cycles, with a capacity retention rate of 68.4% (Fig. 1i and j). In addition, the average coulombic efficiency (CE) of LTO sulfide ASSLBs shows a positive correlation with stacking pressure, whereas the LiIn sulfide ASSLB at 375 MPa exhibits a much lower average CE of 87.4% (Fig. 1e), indicating a greater side reaction during cycling.[39]

To systematically investigate the relationship between electrochemical performance, stress evolution, and mechanical failure during cycling, the pressure behavior of sulfide ASSLBs with NCM95 cathodes and different anodes was studied under various stacking pressures during charging and discharging. As shown in Fig. 2a–c, in LiIn sulfide ASSLBs, the pressure variation is significant and a consistent pressure variation trend is

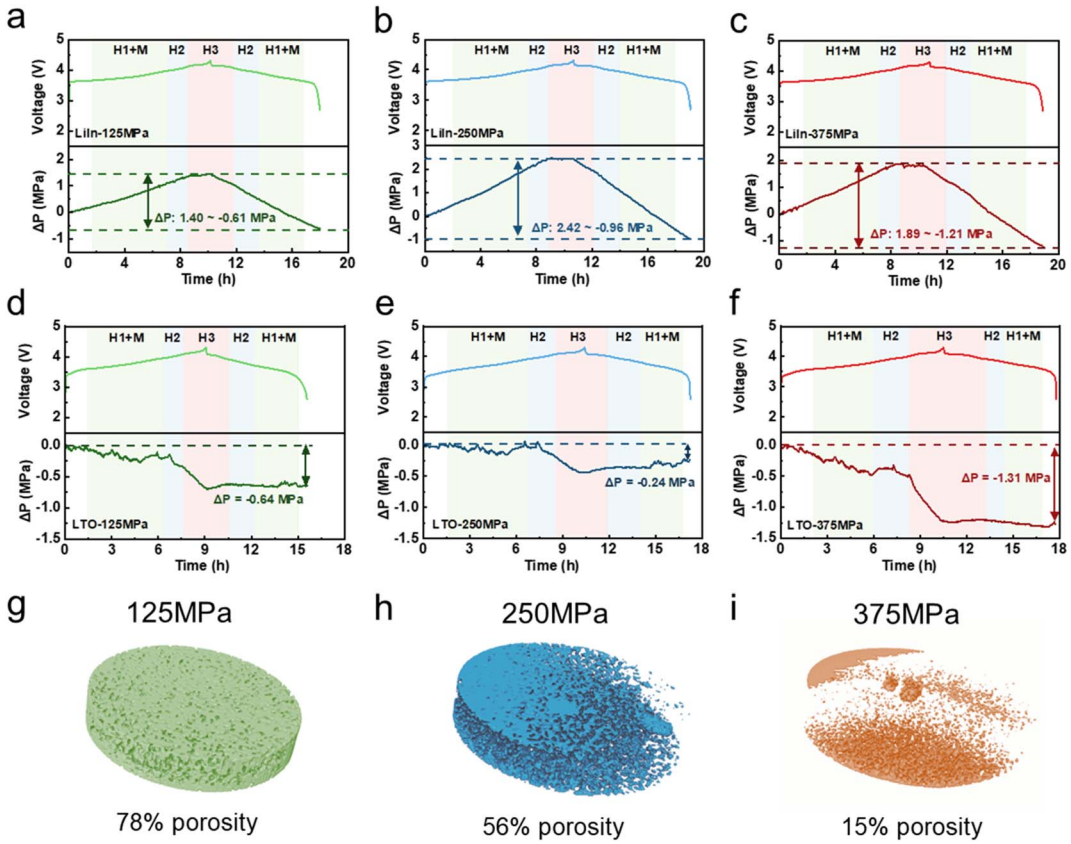

Fig. 2 Pressure changes during charging and discharging. *In situ* pressure measurement curves and voltage profiles of the (a) LiIn-125 MPa, (b) LiIn-250 MPa, (c) LiIn-375 MPa, (d) LTO-125 MPa, (e) LTO-250 MPa, and (f) LTO-375 MPa during the first charging and discharging. (g–i) Three-dimensional nano-CT volume rendering images of the composite cathode under different stacking pressures. The colored regions represent pores.

observed across all tested stacking pressure levels during charging and discharging. Specifically, pressure universally increases during charging and decreases during discharging. This is because the significant volume effect (9–10 vol%) of the lithium alloy anode masks the changes in the cathode material.[30] Furthermore, this is fully consistent with the behavior of lithium metal anodes, which further confirms that the pressure signal primarily originates from the anode.[36] However, the magnitude of these pressure changes is not fixed. Instead, it shows significant differences depending on the initial stacking pressure. When the stacking pressure is 125 MPa, there are certain voids at the solid–solid interfaces inside the battery (Fig. 2g). These voids provide a buffer space for the volume changes of materials during charging and discharging. Consequently, the overall pressure fluctuation during cycling remained within a narrow range from 1.40 MPa to −1.93 MPa in 10 cycles (Fig. 2a and S6a). When the stacking pressure increases to 250 MPa, the solid–solid interfacial voids are fully compressed, enabling tight contact between the electrodes and the sulfide SSE (Fig. 2h). In this state, the stress generated by material volume changes can be efficiently transmitted to the entire battery with almost no buffer loss. Correspondingly, the pressure variation during the 10 cycles ranges from 2.42 MPa to −3.97 MPa (Fig. 2b and S6b). When the stacking pressure is further increased to 375 MPa, internal components of the battery (such as electrodes and sulfide SSE) are compressed to near their mechanical limits, forming a rigid constraint environment (Fig. 2i). On the one hand, this rigid environment inhibits the volume expansion of the anode material during charging (due to limited expansion space), leading to a smaller pressure increase amplitude (1.89 MPa) after charging compared with the LiIn-250 MPa sulfide ASSLB (2.42 MPa). On the other hand, the rigid interface exhibits poor deformability, which allows the volume contraction of the anode during discharge to be more effectively translated into a pressure decrease. As a result, the magnitude of the pressure drop after cycling is further amplified (Fig. 2c and S6c).

To further investigate the pressure evolution during the charging and discharging of the CAM, pressure tests were conducted on sulfide ASSLBs with an LTO anode. For LTO sulfide ASSLBs, the dynamic changes in internal pressure throughout the charging and discharging exhibit a strong and clear correlation with the characteristic phase transitions of the NRLOs (Fig. 2d–f). This is because the LTO anode possesses a "zero-strain" property, with a volume change of less than 0.1% during lithiation and delithiation, meaning it barely contributes to pressure fluctuations.[36] During charging, the pressure decreases as Li^+ ions are deintercalated from the structure of CAM. Subsequently, during the M → H2 phase transition, a temporary increase in pressure is observed. This phenomenon

can be explained by the anisotropic lattice changes. Particularly, the *a*-axis gradually contracts while the *c*-axis expands, leading to a complex strain response that momentarily elevates the pressure. As charging continues into the H2 → H3 phase transition, a rapid decline in pressure occurs. This is primarily due to the cooperative contraction of both the *a*-axis and *c*-axis, which significantly reduces the overall unit cell volume. Notably, the LTO sulfide ASSLBs under 125 MPa exhibit a larger pressure drop than at 250 MPa (Fig. 2d and S7). This is because, at lower stacking pressure, the initial interparticle contact is inherently incomplete. Furthermore, unlike the LiIn alloy anode, LTO does not exhibit significant plasticity or creep behavior that could provide additional self-clamping force to compensate for contact loss. As a result, during repeated cycling, continuous particle rearrangement and interfacial loosening occur, leading to more pronounced stress relaxation within the electrode layers, which further results in an increased internal pressure drop in the sulfide ASSLBs.[31]

In summary, different anode materials, particularly zero-strain LTO and Li–In alloy, exhibit distinct volumetric behaviors during the charging and discharging of the sulfide ASSLBs. Notably, the internal pressure in LTO sulfide ASSLBs exhibits relatively mild variations, and their electrochemical performance improves steadily with increasing stacking pressure. In contrast, the significant cyclic volume changes of the LiIn anode, exacerbated by the applied stacking pressure, result in substantial fluctuations in internal pressure. The synchronous occurrence of drastic internal pressure fluctuations and rapid electrochemical performance degradation in LiIn sulfide ASSLBs suggests that mechanical failure may be a critical factor contributing to performance decline. The specific forms and mechanisms through which the pressure behavior of the Li–In anode affects the cathode, leading to mechanical failure in sulfide ASSLBs, require further investigation.

To investigate the impact of pressure changes induced by the LiIn alloy anode on the mechanical failure of NRLOs in sulfide ASSLBs, HRTEM was performed on NCM95 after the first charging and discharging. Fast Fourier Transform (FFT) was applied to the selected regions, and the corresponding crystal planes were identified based on interplanar spacings and angles. As shown in Fig. 3b and S8, the NCM95, pre-treated with a stacking pressure of 250 MPa, maintains a well-ordered layered crystal structure with the characteristic $R\bar{3}m$ space group (Fig. 3a) before undergoing any electrochemical cycling. Following the initial charging and discharging of the LiIn-125 MPa sulfide ASSLB, as shown in Fig. S9a, the majority of the lattice on the surface of the NCM95 sample retains a relatively intact layered structure. Notably, no significant lattice distortion or dislocation is observed in most regions, indicating that cycling under a relatively low stacking pressure (125 MPa) does not induce substantial mechanical damage to the NCM95 lattice, thus preserving the stability of the crystal structure. When the stacking pressure is increased to 250 MPa (Fig. 3c and S9b), the surface lattice of NCM95 displays marked variations in structural integrity across different regions. Some areas maintain a well-preserved layered structure, with clear and continuous lattice fringes consistent with the $R\bar{3}m$ space group (region I). However, region II exhibits noticeable atomic displacement within the lattice, where the lattice fringes appear slightly blurred, and the original regular atomic arrangement is disrupted (Fig. S10).[40] This phenomenon occurs because under high stacking pressure, NCM95 undergoes significant pressure variation (Fig. 2b), leading to partial lattice deformation due to localized stress concentration. As the stacking pressure further increases to 375 MPa, the mechanical damage to NCM95 becomes more severe (Fig. S9c). At this pressure level, only a small portion of the lattice in the entire observation region retains its original layered structure, with the corresponding lattice fringes being discontinuous and weak. In contrast, a large area of the lattice undergoes significant shear deformation, resulting in twisted, broken, and even completely disordered lattice fringes, with the layered structure nearly lost. This phenomenon can impede Li^+ transport, thereby resulting in the poor rate capability of the LiIn-375 MPa sulfide ASSLB.[41]

Furthermore, the X-ray diffractometer (XRD) results provide further evidence for the changes in the lattice structure. Specifically, the variation of the (003) peak is indicative of structural changes along the *c*-axis of the lattice.[42] As the stacking pressure increases, the (003) peak continuously shifts toward higher 2θ angles, accompanied by a sharp decrease in the unit cell parameter *c*-axis. During the lattice collapse process, a "peak broadening" phenomenon is also observed, which indicates that the long-range order of the lattice is severely disrupted (Fig. S11).

This structural change not only impedes the transport of Li^+ but also leads to the generation of lattice oxygen, both of which are key factors leading to battery capacity decay and cycle stability degradation. As shown in Fig. 3d and e, with the gradual increase in stacking pressure applied during battery assembly, the amount of oxygen released from the NCM95 cathode material during the first charging and discharging shows a clear upward trend. This progressive increase in oxygen release directly reflects the aggravation of lattice damage in NCM95. Under higher pressure, the layered structure of the material is more likely to collapse, and the lattice oxygen that was originally stably bound in the crystal framework becomes detached and is released in the form of free oxygen. To further verify the loss of lattice oxygen, electron paramagnetic resonance (EPR) tests were conducted on NCM95 samples treated with different stacking pressures after the first charging and discharging. The results (Fig. 3g) indicate that as the stacking pressure rises, the signal intensity corresponding to oxygen vacancies in the material gradually increases. The O 1s spectrum (Fig. S12) further confirms that as the stacking pressure increases, the content of oxygen vacancies (531.8 eV) increases, while the content of lattice oxygen (527.9 eV) decreases.[43] In addition, the Ni $2p_{3/2}$ peak shifts to lower binding energy, and the average valence state of Ni on the material surface decreases (*e.g.*, from Ni^{3+}/Ni^{4+} to lower valence states such as Ni^{2+}), serving to compensate for the oxygen loss in the lattice (Fig. 3h). However, Ni^{2+} with lower valence states have poor ability to participate in the redox reactions required for Li^+ intercalation/deintercalation, leading to a sharp decline in the specific discharge capacity of the battery.[44,45] X-ray photoelectron

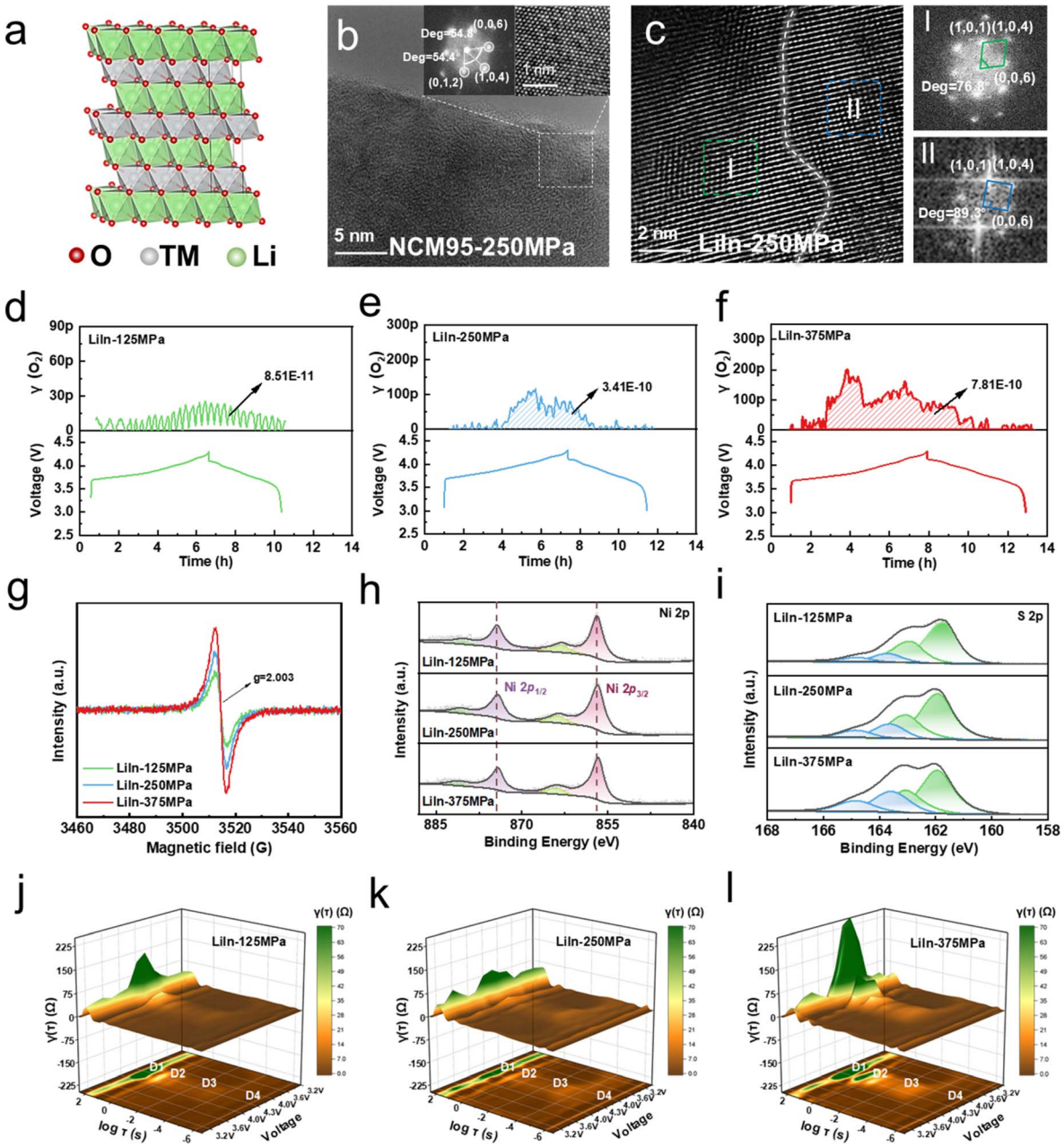

Fig. 3 Mechanical degradation mechanism of NRLOs in sulfide ASSLBs. (a) Schematic diagram of the layered NCM95 structure. (b) HRTEM images and selected area FFT, iFFT of NCM95 after standing at 250 MPa. (c) CAM surface version HRTEM and corresponding FFT of LiIn-250 MPa after the first charging and discharging. O_2 production of (d) LiIn-125 MPa, (e) LiIn-250 MPa, and (f) LiIn-375 MPa. (g) EPR results of NCM95 after the first charging and discharging under different stacking pressures. The XPS spectra of (h) Ni 2p and (i) S 2p for the composite cathode after the first charging and discharging under different stacking pressures. DRT of (j) LiIn-125 MPa, (k) LiIn-250 MPa, and (l) LiIn-375 MPa during the first charging and discharging.

spectroscopy (XPS) was performed on the sulfide SSE after the first charging and discharging to analyze the decomposition behavior of the sulfide SSE. As shown in Fig. 3i and Table S2, due to the oxidation of lattice oxygen, apart from the main signal associated with PS_4^{3-} (161.7 eV), the decomposition product P_2S_x (163.2 eV) is also detected.[46] Moreover, the content of P_2S_x increases as the stacking pressure rises. Furthermore, as the stacking pressure increases, no significant change is observed in the crystal structure of the sulfide SSE, while the ionic conductivity improves slightly and the decomposition potential decreases noticeably (Fig. S13). This phenomenon can be attributed to the increase in dislocation density within the crystal structure of the sulfide SSE under higher pressure.[25,29] The escape of lattice oxygen caused by lattice deformation and the decomposition of the sulfide SSE are exactly the reasons for the low ICE (75.6%) of the LiIn-375 MPa sulfide ASSLB. These results indicate that the cathode material of the LiIn sulfide

ASSLBs experiences severe mechanical–electrochemical failure at the very early stage of cycling.

HRTEM analysis was also performed on NCM95 of LTO sulfide ASSLBs after the first charging and discharging, as shown in Fig. S14. In contrast to sulfide ASSLBs with LiIn anodes, those equipped with LTO anodes exhibit markedly less structural degradation of the cathode after the first charging and discharging. Even when the stacking pressure is increased to 375 MPa, only minimal lattice distortion is observed on the surface of NRLO in LTO sulfide ASSLBs. While oxygen release from the NCM95 cathode shows a significant increasing trend with stacking pressure in LTO sulfide ASSLBs, the extent remains notably subdued compared to LiIn sulfide ASSLBs. This difference can be attributed to the relatively modest pressure variation within the LTO sulfide ASSLBs. Consequently, although increasing the stacking pressure does exacerbate cathode failure in LTO sulfide ASSLBs, the degree of degradation under equivalent pressure conditions is substantially less severe compared to that of LiIn sulfide ASSLBs.

To gain in-depth insights into the influence of stacking pressure on Li^+ transport behavior of LiIn sulfide ASSLBs, *in situ* EIS measurements were performed during the first charging and discharging (Fig. S15), and the DRT technique was further employed to analyze the evolution of interfacial impedance. In Fig. 3j–l, D1 represents the diffusion process, D2 denotes the charge transfer resistance at the electrode surface (R_{ct}), D3 corresponds to the Li^+ transport process at the electrode interface, and D4 reflects the grain boundary ion conduction of the sulfide SSE (R_{SSE}).[47] At relatively low stacking pressure (125 MPa), the solid–solid contact between components within the sulfide SSE is inadequate, resulting in a pronounced D1 peak that indicates sluggish Li^+ diffusion kinetics (Fig. 3j) and a significant charge transfer resistance. When the stacking pressure is increased to 250 MPa, the applied pressure effectively compresses the internal gaps between particles, promoting tighter solid–solid contact. This enhanced interfacial contact reduces the diffusion resistance of Li^+ and improves the electrochemical reaction kinetics, as evidenced by the decrease in R_{ct} (Fig. 3k). However, when the stacking pressure is further raised to 375 MPa, lattice distortion occurs in the NRLOs, leading to a significant increase in both Li^+ diffusion impedance and R_{ct} (Fig. 3l). In addition, with the increase of stacking pressure, D3 (related to interface Li^+ transport) shows an enhanced relaxation peak intensity and a gradual voltage-dependent peak shift associated with side reactions, indicating a significant increase in side reaction products. Furthermore, as the stacking pressure increases, R_{SSE} (D4) gradually increases, which is caused by the oxidative decomposition of the sulfide SSE under high stacking pressure.[48] Similarly, as shown in Fig. S16, during the initial stages of charging, the Li^+ diffusion coefficient (D_{Li^+}) increases noticeably with increasing stacking pressure. However, at high states of charge (SOC), the LiIn-375 MPa sulfide ASSLB exhibits a significantly lower D_{Li^+} compared to other samples, further indicating that excessive stacking pressure induces lattice distortion, which hinders Li^+ transport.

The impedance during the cycling process was measured and fitted using the equivalent circuit depicted in Fig. S17.[49,50] The fitting results are presented in Fig. S18 and S19, and Table S1. The LiIn-125 MPa sulfide ASSLB demonstrates a unique behavior during its initial cycling phase, characterized by a decrease in interfacial impedance. This trend aligns with the observed discharge specific capacity, which initially rises before subsequently declining. The initial decrease in impedance can be attributed to interfacial side reactions that occur during the early stages of cycling. These reactions produce byproducts that effectively fill the gaps at the solid–solid interface, thereby enhancing charge transfer efficiency. In contrast, the LiIn-250 MPa and LiIn-375 MPa sulfide ASSLBs exhibit a gradual increase in interfacial impedance as cycling progresses. Notably, the LiIn-375 MPa variant experiences a pronounced rise in impedance, which correlates with a sharp decline in battery capacity. This suggests that the higher-pressure conditions may exacerbate interfacial degradation, leading to less effective charge transfer and ultimately compromising the battery's performance.

To gain a comprehensive understanding of the effect of stacking pressure in LiIn sulfide ASSLBs on the interfacial properties and crystal structure of Ni-rich cathode particles, HRTEM characterization was performed on the composite cathode after 200 cycles. FFT analysis was conducted on the selected regions, and the corresponding crystal planes were identified based on interplanar spacing and angles. As shown in Fig. 4a, the structure of NRLOs after 200 cycles under low pressure exhibits minimal degradation and retains a relatively intact layered structure. When the stacking pressure increases to 250 MPa, partial rock salt phase structure ($Fm\bar{3}m$) is formed on the material surface (Fig. 4b), significantly hindering the diffusion of Li^+ along the ab plane. Furthermore, with a further increase in stacking pressure, the rock salt phase structure on the surface continues to expand (Fig. 4c). This phenomenon is attributed to lattice deformation and the release of lattice oxygen induced by excessive pressure. In Fig. 4a–d, after 200 cycles, the lattice spacing decreases continuously from 0.211 nm to 0.171 nm as stacking pressure increases. This continuous reduction in interplanar spacing is primarily due to the cumulative effects of mechanical stress and chemical changes during charging and discharging. Under higher stacking pressure, Ni-rich cathode particles experience greater compressive forces, coupled with repeated volume expansion and contraction during Li^+ insertion and extraction. This results in significant localized stress concentration within the lattice, leading to lattice distortion and loss of lattice oxygen, ultimately causing the collapse of the crystal structure.

Fig. 4e illustrates the variation in the surface Ni valence state of cycled NRLOs with increasing stacking pressure. As stacking pressure rises, a clear decrease in the average surface Ni valence is observed, further confirming the degradation of the lattice structure. Moreover, EPR and the O 1s XPS spectra (Fig. S20) provide additional evidence that higher stacking pressure leads to a reduction in lattice oxygen and a notable increase in oxygen vacancies. The failure behavior of the sulfide SSE after cycling was also analyzed. As shown in Fig. 4f and Table S3, after 200

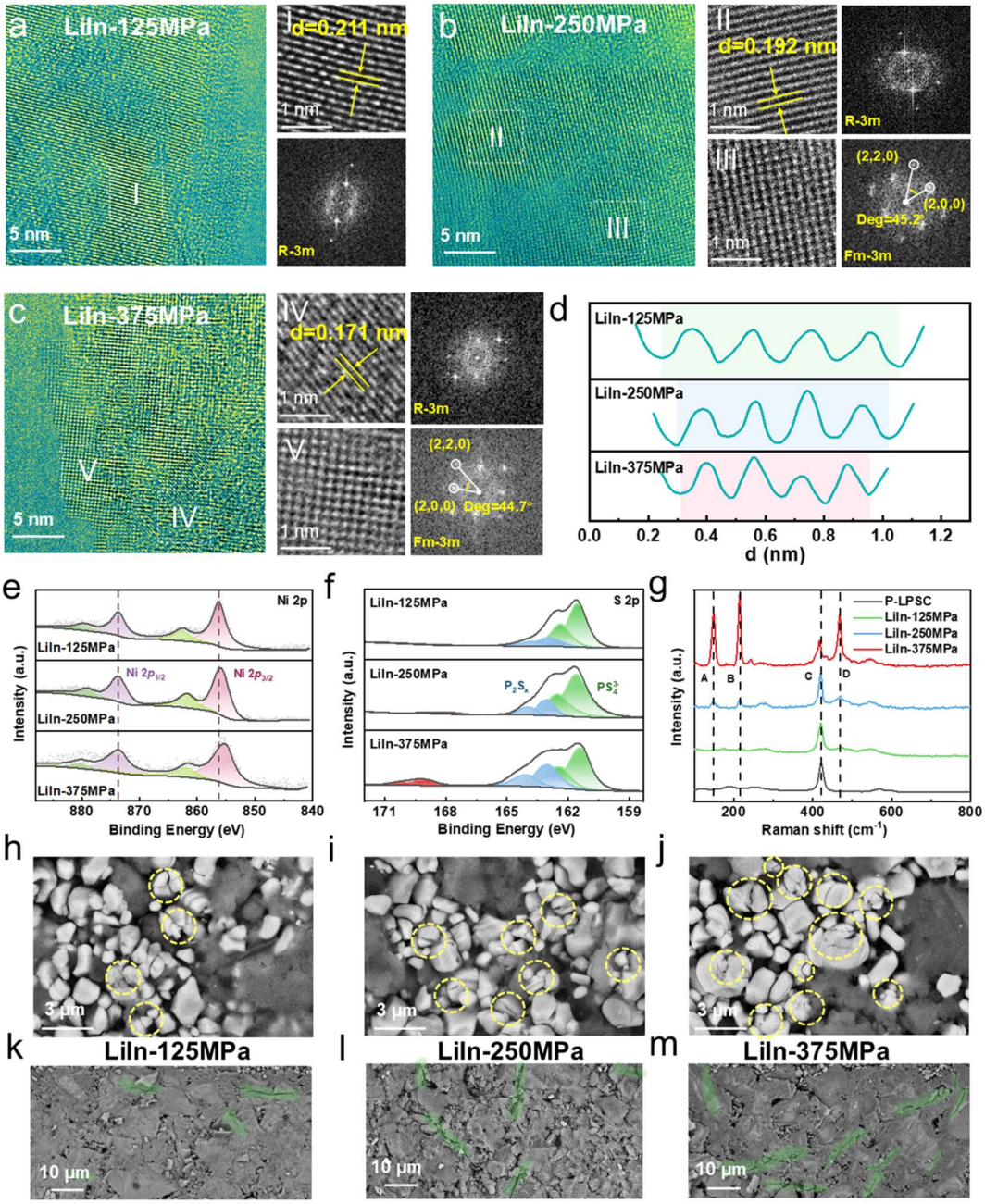

Fig. 4 Interfacial variation of NRLOs and the sulfide SSE after cycling. CAM surface version HRTEM and corresponding FFT for the NCM95 s of (a) LiIn-125 MPa, (b) LiIn-250 MPa, and (c) LiIn-375 MPa after 200 cycles. (d) Line profiles across crystal planes of different NCM95 samples. The XPS spectra of (e) Ni 2p and (f) S 2p for the composite cathodes after 200 cycles. (g) Raman spectra of the composite cathodes after 200 cycles. (h–j) Electron backscattered diffraction (EBSD) of the composite cathodes after 200 cycles. (k–m) EBSD of the composite cathode and sulfide SSE cross-sections after 200 cycles.

cycles under low stacking pressure (125 MPa), only a small amount of by-product is generated in the sulfide SSE. With the increase in stacking pressure, the sulfide SSE not only produces more P_2S_x but also generates a large quantity of SO_x, further degrading the Li_6PS_5Cl structure and causing rapid capacity fade. Raman spectroscopy results provide more detailed information about chemical bonds (Fig. 4g). Consistent with the XPS results, as the stacking pressure increases, the intensity of the PS_4^{3-} peak (C) gradually decreases, while the intensity of the P_2S_x peak (A) increases progressively. Notably, a significant increase in the intensity of –S–S– bonds (B and D) is observed with the rise in stacking pressure. The extensive presence of –S–S– bonds, which is associated with structural disordering of the sulfide SSE, severely disrupts the Li^+ conduction channels within the electrolyte.[51]

Furthermore, at the macroscopic level, optical images of the cycled electrodes reveal increasingly severe cracking with higher stacking pressure. Specifically, the electrode sheet of the LiIn-375 MPa sulfide ASSLB even exhibits interlayer delamination (Fig. S21). At the microscopic scale, numerous microcracks are

observed on the surface of the cycled NRLOs, with the stacking pressure rising (Fig. 4h–j). Concurrently, the sulfide SSE layer also shows progressively expanding cracks under increasing stacking pressure (Fig. 4k–m). The degradation of this micro–macro synergistic electrode structure is primarily attributed to the accumulation of mechanical stress during prolonged cycling, with high stacking pressure exacerbating this cumulative effect, which leads to a sharp decline in the cycling stability and rate performance of sulfide ASSLBs.

Conclusions

This study investigates the regulatory mechanism of stacking pressure on the mechanical failure of NRLOs in sulfide ASSLBs. Through multi-scale characterization and electrochemical analysis, the dual role of stacking pressure in sulfide ASSLBs is elucidated. On the one hand, increased stacking pressure compresses interfacial voids and reduces Li^+ transport resistance, significantly enhancing discharge capacity and rate performance. On the other hand, excessively high stacking pressure exacerbates the pronounced volume changes of the LiIn alloy anode, leading to mechanical degradation of the cathode lattice and compromising the stability of the solid electrolyte, which results in rapid capacity fading and increased polarization. In contrast, the near-zero strain characteristic of the LTO anode effectively mitigates internal stress fluctuations, enabling stable cycling performance even under 375 MPa. Furthermore, an in-depth investigation into the mechanism of mechanical degradation in LiIn sulfide ASSLBs reveals that significant pressure variations during cycling induce shear deformation and structural collapse of the layered framework in the NRLOs. This process is accompanied by a marked increase in oxygen vacancies and a reduction in the average nickel valence state (from Ni^{3+}/Ni^{4+} to Ni^{2+}), which impedes the intercalation and deintercalation of Li^+. Concurrently, the release of lattice oxygen accelerates the oxidative decomposition of the sulfide SSE, generating deleterious species such as P_2S_x and SO_x. These byproducts further obstruct Li^+ transport pathways and increase grain boundary impedance. Additionally, this degradation process promotes macroscopic electrode delamination and microscopic cracking of cathode particles, collectively resulting in a capacity retention of only 29.2% after 100 cycles. Future work will focus on precisely identifying the critical stacking pressure leading to failure using advanced modelling and experiments. Subsequently, improved cathode interfaces with flexible coatings will be developed to manage stress. Additionally, adaptive battery structures will be designed to automatically maintain optimal internal pressure. These strategies seek to reduce the required stacking pressure in such batteries, thereby facilitating their adaptation to industrial manufacturing processes.

Author contributions

Yiman Feng proposed the concepts, designed and carried out the experiments and wrote the original manuscript. Jiexi Wang proposed the concepts and revised the original manuscript. Gui Luo, Duo Deng, Hui Duan, and Zhixing Wang provided guidance on the design in the experiment. Wenjie Peng, Wenchao Zhang, Feixiang Wu, Xing Ou, and Junchao Zheng supervised the work.

Conflicts of interest

There are no conflicts to declare.

Data availability

The data that support the findings of this study are available within the article and its supplementary information (SI). Supplementary information: experimental section and some additional supplementary experimental data: schematic diagram of sulfide ASSLB assembly; rate performance of sulfide ASSLBs; pressure change of different sulfide ASSLBs during the cycling; HRTEM of CAM after standing at 250 MPa or after the first cycling; XRD and XPS for the composite cathodes after first cycling under different stacking pressure; LSV curves of sulfide SSE under different stacking pressures; *in situ* EIS profiles of sulfide ASSLBs during the first charging and after different cycles; XPS, EPR and EBSD for the composite cathode after 200 cycles under different stacking pressure. See DOI: https://doi.org/10.1039/d5sc09321j.

Acknowledgements

This work was supported by the National Natural Science Foundation of China (No. 52122407, No. 22409217), and the Science and Technology Innovation Program of Hunan Province (No. 2022RC3048, No. 2024QK2004). We also thank BASF Shanshan Battery Material Co., Ltd for financial support. During the preparation of this manuscript, the authors used DeepSeek-V3 and Gpt-4o-mini to improve its spelling, grammar, clarity and overall readability. After using these tools or services, the authors reviewed and edited the content as needed and take full responsibility for the content of the publication.

References

1 H. Yuan, W. Lin, S. Chen, C. Tian, T. Huang and A. Yu, *ACS Nano*, 2025, **19**, 2570–2580.
2 Y. Dai, Z. Hou, G. Luo, D. Deng, W. Peng, Z. Wang, H. Guo, X. Li, G. Yan, H. Duan, W. Zhang and J. Wang, *Chem. Sci.*, 2024, **15**, 12964–12972.
3 C. Kim, Y. Li, I. Jang, W. Wu, Y. Su, H. M. Meyer, J. Keum, J. Nanda and G. Yang, *Adv. Mater.*, 2025, **37**, 2502300.
4 X. Zhang, J. Yang, E. Deng, J. Huang, M. Jin, P. Jiang and X. Lu, *Energy Storage Mater.*, 2025, **79**, 104339.
5 I. P. Oyekunle, E. Truong, T. P. Poudel, Y. Chen, Y. Jin, I. A. Ojelade, M. J. Deck, B. Ogbolu, Md. M. Islam, P. K. Ojha, J. S. R. Vellore Winfred, D. Hou, H. Xiong, C. Huang and Y.-Y. Hu, *Chem. Sci.*, 2025, **16**, 10372–10385.
6 Z. Su, Q. Zhou, J. Jin, S. Yang, G. Li and J. Zhang, *Adv. Sci.*, 2024, **11**, 2407798.

7 D. Sun, W. Li, Y. Wang, J. Ju, P. Han, S. Dong, J. Ma and G. Cui, *Chem. Sci.*, 2025, **16**, 10289–10295.
8 P. Lu, S. Gong, C. Wang, Z. Yu, Y. Huang, T. Ma, J. Lian, Z. Jiang, L. Chen, H. Li and F. Wu, *ACS Nano*, 2024, **18**, 7334–7345.
9 B. Zhang, Y. Yan, Z. Chen, S. Yang and Z. Yang, *Chin. Chem. Lett.*, 2025, 111952.
10 Q. Zhang, J. Wang, Y. Chu, W. Huang, X. Huang, X. Xiao, L. Ma, T. Liu, K. Amine, J. Lu and C. Yang, *Nat. Energy*, 2025, **10**, 1001–1012.
11 L. Li, Y. Huang, Z. Liu, N. Zhao, H. Liang, M. Zhou, K. Zou, L. Tan and T. Ning, *Chin. Chem. Lett.*, 2025, 111079.
12 J. Shi, P. Li, K. Han, D. Sun, W. Zhao, Z. Liu, G. Liang, K. Davey, Z. Guo and X. Qu, *Energy Storage Mater.*, 2022, **51**, 306–316.
13 Y. Li, C. Kim, Y. Cho, A. L. Musgrove, G. D. Parker, Y.-F. Su, R. L. Sacci, X.-Y. Yu, T. Zawodzinski, J. Nanda and G. Yang, *Energy Storage Mater.*, 2025, **80**, 104385.
14 J. Y. Lee, S. Noh, J. Y. Seong, S. Lee and Y. J. Park, *ACS Appl. Mater. Interfaces*, 2023, **15**, 12998–13011.
15 R. S. Negi, Y. Yusim, R. Pan, S. Ahmed, K. Volz, R. Takata, F. Schmidt, A. Henss and M. T. Elm, *Adv. Mater. Inter.*, 2022, **9**, 2101428.
16 S. H. Jung, K. Oh, Y. J. Nam, D. Y. Oh, P. Brüner, K. Kang and Y. S. Jung, *Chem. Mater.*, 2018, **30**, 8190–8200.
17 X. Wang, M. Zhou, Y. Deng, Z. Liu, H. Dong, P. Yan and R. Liu, *Chin. Chem. Lett.*, 2024, 110307.
18 Y. Feng, J. Liu, Z. Wei, S. Yao, G. Chen and F. Du, *Angew. Chem., Int. Ed.*, 2025, **64**, e202507247.
19 M. Ji, D. Liu, B. Peng, Y. Liu, X. Liao and D. Qu, *Energy Storage Mater.*, 2025, **79**, 104301.
20 H. Xu, Y. Su, C. Zheng, Y. Wang, Y. Tong, Z. Yang and J. Hu, *Chin. Chem. Lett.*, 2024, **35**, 109173.
21 D. H. S. Tan, Y.-T. Chen, H. Yang, W. Bao, B. Sreenarayanan, J.-M. Doux, W. Li, B. Lu, S.-Y. Ham, B. Sayahpour, J. Scharf, E. A. Wu, G. Deysher, H. E. Han, H. J. Hah, H. Jeong, J. B. Lee, Z. Chen and Y. S. Meng, *Science*, 2021, **373**, 1494–1499.
22 A. Song, W. Zhang, H. Guo, L. Dong, T. Jin, C. Shen and K. Xie, *Adv. Energy Mater.*, 2023, **13**, 2301464.
23 S. Jing, Y. Lu, Y. Huang, H. Liu, Y. Shen, W. Kuang, H. Shen, S. Liu, Z. Zhang and F. Liu, *Adv. Mater.*, 2024, 2312305.
24 Y. Ma, H. Qu, W. Wang, Y. Yu, X. Zhang, B. Li and L. Wang, *Adv. Funct. Mater.*, 2023, **33**, 2211648.
25 D. Lee, Y. Shim, E. Choi, K. Kim, J.-S. Yu, S. H. Choi, W. Cho and D.-J. Yoo, *Joule*, 2025, **9**, 102046.
26 G.-T. Park, D. R. Yoon, U.-H. Kim, B. Namkoong, J. Lee, M. M. Wang, A. C. Lee, X. W. Gu, W. C. Chueh, C. S. Yoon and Y.-K. Sun, *Energy Environ. Sci.*, 2021, **14**, 6616–6626.
27 R. Koerver, W. Zhang, L. De Biasi, S. Schweidler, A. O. Kondrakov, S. Kolling, T. Brezesinski, P. Hartmann, W. G. Zeier and J. Janek, *Energy Environ. Sci.*, 2018, **11**, 2142–2158.
28 C. Wei, X. Liu, C. Yu, S. Chen, S. Chen, S. Cheng and J. Xie, *Chin. Chem. Lett.*, 2023, **34**, 107859.
29 Q. Li, H. Liu, Y. Ye, K. J. Li, F. Wu, L. Li and R. Chen, *Nat. Energy*, 2025, 1–10.
30 X. Hu, Z. Zhang, X. Zhang, Y. Wang, X. Yang, X. Wang, M. Fayena-Greenstein, H. A. Yehezkel, S. Langford, D. Zhou, B. Li, G. Wang and D. Aurbach, *Nat. Rev. Mater.*, 2024, **9**, 305–320.
31 H. Xu, S. Yang and B. Li, *Adv. Energy Mater.*, 2024, 2303539.
32 J. Gu, Z. Liang, J. Shi and Y. Yang, *Adv. Energy Mater.*, 2023, **13**, 2203153.
33 Z. Huang, H. Lyu, L. C. Greenburg, Y. Cui and Z. Bao, *Nat. Energy*, 2025, **10**, 811–823.
34 P. Zhang, X. Wang, Y. Zhang, Y. Wei, N. Shen, S. Chen and B. Xu, *Adv. Funct. Mater.*, 2024, **34**, 2402307.
35 F. Zhang, Y. Guo, L. Zhang, P. Jia, X. Liu, P. Qiu, H. Zhang and J. Huang, *eTransportation*, 2023, **15**, 100220.
36 J. Kang, H. R. Shin, J. Yun, S. Kim, B. Kim, K. Lee, Y. Lim and J.-W. Lee, *Energy Storage Mater.*, 2023, **63**, 103049.
37 X. Zheng, Z. Xue, H. Hao, Y. Cho, Y. Li, C. Kim, P. Czaja, S. S. Lee, S. Bone, E. Spielman, Z. Jiang, X. W. Gu, J. N. Weker, G. Yang and J. Nanda, *Sci. Adv.*, 2025, **11**(41), eady7189.
38 K.-Y. Park, J.-W. Park, W. M. Seong, K. Yoon, T.-H. Hwang, K.-H. Ko, J.-H. Han, Y. Jaedong and K. Kang, *J. Power Sources*, 2020, **468**, 228369.
39 Y. Zheng, S. Zhang, J. Ma, F. Sun, M. Osenberg, A. Hilger, H. Markötter, F. Wilde, I. Manke, Z. Hu and G. Cui, *Sci. Bull.*, 2023, **68**, 813–825.
40 Q. Zhang, L. Y. Zhang, C. H. Jin, Y. M. Wang and F. Lin, *Ultramicroscopy*, 2019, **202**, 114–120.
41 P. J. Kwon, C. Juarez-Yescas, H. Jeong, S. Moradi, E. Gao, D. Lawrence, B. Zahiri and P. V. Braun, *ACS Energy Lett.*, 2024, **9**, 4746–4752.
42 M. Zhang, W. Huang, J. Tang, Z. Liu, C. Sheng, X. Sun, H. Zhong, S. Xu, W. Ning, X. Xiao, T. Liu, S. Guo and H. Zhou, *J. Am. Chem. Soc.*, 2025, **147**, 1563–1573.
43 L. Yuan, W. Peng, Z. Zhan, J. Wang, Y. Feng, Y. Yan, R. Yu, C. Wang, Z. Wang, H. Guo, G. Yan, G. Li, H. Duan, J. Wang and X. Sun, *Angew. Chem., Int. Ed.*, 2025, e202508605.
44 Y. Dai, J. Tan, Z. Hou, B. You, G. Luo, D. Deng, W. Peng, Z. Wang, H. Guo, X. Li, G. Yan, H. Duan, Y. Wang, F. Wu and J. Wang, *ACS Nano*, 2024, **18**, 22518–22532.
45 S. Huang, B. Luo, Z. Zhang, Q. Wang, G. Yu, X. Bu, Z. Huang, X. Wang, W.-L. Song, J. Zhang and S. Jiao, *Chin. Chem. Lett.*, 2024, 110729.
46 M. S. Nafis, Z. Liang, S. Lee and C. Ban, *Nano Energy*, 2025, **133**, 110447.
47 A. Maradesa, B. Py, J. Huang, Y. Lu, P. Iurilli, A. Mrozinski, H. M. Law, Y. Wang, Z. Wang, J. Li, S. Xu, Q. Meyer, J. Liu, C. Brivio, A. Gavrilyuk, K. Kobayashi, A. Bertei, N. J. Williams, C. Zhao, M. Danzer, M. Zic, P. Wu, V. Yrjänä, S. Pereverzyev, Y. Chen, A. Weber, S. V. Kalinin, J. P. Schmidt, Y. Tsur, B. A. Boukamp, Q. Zhang, M. Gaberščček, R. O'Hayre and F. Ciucci, *Joule*, 2024, **8**, 1958–1981.
48 P. Lu, Y. Wu, D. Wu, F. Song, T. Ma, W. Yan, X. Zhu, F. Guo, J. Lu, J. Peng, L. Chen, H. Li and F. Wu, *Energy Storage Mater.*, 2024, **67**, 103316.

49 J. Zhang, C. Zheng, L. Li, Y. Xia, H. Huang, Y. Gan, C. Liang, X. He, X. Tao and W. Zhang, *Adv. Energy Mater.*, 2020, **10**, 1903311.
50 J. Wang, S. Zhao, A. Zhang, H. Zhuo, G. Zhang, F. Han, Y. Zhang, L. Tang, R. Yang, L. Wang and S. Lu, *ACS Appl. Energy Mater.*, 2023, **6**, 3671–3681.
51 Y. Nikodimos, C.-J. Huang, B. W. Taklu, W.-N. Su and B. J. Hwang, *Energy Environ. Sci.*, 2022, **15**, 991–1033.